Title
Surface tension models for a multi-material ALE code with AMR

Authors
Liu, Wangyi
Koniges, Alice
Gott, Kevin
et al.

Publication Date
2017-06-01

DOI
10.1016/j.compfluid.2017.01.016

Peer reviewed

Computers and Fluids 151 (2017) 91–101

Contents lists available at ScienceDirect

Computers and Fluids

journal homepage: www.elsevier.com/locate/compfluid

Surface tension models for a multi-material ALE code with AMR

Wangyi Liu[a,c], Alice Koniges[a,*], Kevin Gott[a], David Eder[b], John Barnard[b], Alex Friedman[b], Nathan Masters[b], Aaron Fisher[b]

[a] Lawrence Berkeley National Laboratory, United States
[b] Lawrence Livermore National Laboratory, United States
[c] Google, Mountain View, CA, United States

ARTICLE INFO

Article history:
Received 9 March 2016
Revised 16 December 2016
Accepted 17 January 2017
Available online 30 January 2017

Keywords:
Surface tension
ALE
AMR
Multi-physics modeling
Interface reconstruction
Lithography

ABSTRACT

A number of surface tension models have been implemented in a 3D multi-physics multi-material code, ALE–AMR, which combines Arbitrary Lagrangian Eulerian (ALE) hydrodynamics with Adaptive Mesh Refinement (AMR). ALE–AMR is unique in its ability to model hot radiating plasmas, cold fragmenting solids, and most recently, the deformation of molten material. The surface tension models implemented include a diffuse interface approach with special numerical techniques to remove parasitic flow and a height function approach in conjunction with a volume-fraction interface reconstruction package. These surface tension models are benchmarked with a variety of test problems. Based on the results, the height function approach using volume fractions was chosen to simulate droplet dynamics associated with extreme ultraviolet (EUV) lithography.

1. Introduction

A traditional means of modeling plasma in the high energy density regime is through a fluid description with an ALE (Arbitrary Lagrangian Eulerian) methodology, due to the Lagrangian formulation's ability to deal with large displacements and the mesh-untangling capabilities of the ALE method. Examples of these codes for inertial confinement fusion (ICF) include CHIC, Lasnex, Hydra, and FCI2 [1–4]. Generally, in an ALE method, the pure Lagrangian time-advance phase is followed by a remap step. The Eulerian part of the method comes from the re-map phase, whereby cells that have been skewed are returned close to the original mesh, and thus close to a static Eulerian grid. Without some sort of remap, Lagrange steps can lead to a poor mesh which causes minuscule time steps and hampers the code's ability to progress forward in time.

Recently, we described our work on combining ALE and Adaptive Mesh Refinement (AMR) [5]. The introduction of AMR into the more traditional ALE formulation allows users to choose the appropriate method given the geometry of the problem as well as the physics of the material states in the problem. Our AMR treatment of the flow follows the pioneering methods such as those by Colella [6]. Building on the studies of incorporating ALE and AMR for gas-dynamics [7] using the Structured Adaptive Mesh Refinement Application Interface (SAMRAI) [8], we have developed a fully featured modeling code, ALE–AMR. Our code allows for a variety of gridding treatments, including fully Lagrangian, fully Eulerian (which maps back to the original grid after every step), ALE (which maps to a straightened grid when needed or desired) and any number of levels of mesh refinement. The code adapts traditional cell-centered AMR discretization methods for staggered meshes by solving position and velocity on nodes while maintaining cell-centered descriptions of density and other thermodynamic quantities [7]. An important part of ALE–AMR is contained within the multi-material formulation and the corresponding interface reconstruction capability that provides the flexibility to relax the need of material boundaries to correspond to zone boundaries [9]. This capability is crucial to modeling very complex geometries as well as allowing for a VOF approach and the breakup of materials during simulations. Another important inclusion in ALE–AMR is an implementation of an anisotropic stress tensor. This full tensor is often neglected in traditional radiation-hydrodynamic codes that are not focused towards the lower temperature regimes where surface tension begins to play a role.

ALE–AMR was used as the primary tool for predicting and mitigating damage to NIF optics and diagnostics from debris and shrapnel during the National Ignition Campaign (2008 – 2012) [10]. The code was also used to model ion accelerator targets for warm dense matter experiments [11]. The unique development of ALE–AMR allows simulations of laser or ion experiments that include

* Corresponding author.
E-mail address: aekoniges@lbl.gov (A. Koniges).

http://dx.doi.org/10.1016/j.compfluid.2017.01.016
0045-7930/

the entire target and typically have extreme variations in density and temperature [12]. In these simulations, which range from hot radiating plasmas to cold fragmenting solids, the spatial and temporal scales are also extreme. For example, we have used up to six levels of refinement, which corresponds to a volume ratio of approximately 10^7 to 1 between the largest to smallest zone [13]. More recently the code is being used to model EUV lithography experiments using laser heated droplets [14]. In EUV lithography, the effects of surface tension are significant, which motivated the research detailed in this paper.

The surface tension modeling techniques of interest to our work can be grouped into three categories: energy minimization, sharp interface and diffuse interface. Energy minimization methods calculate the surface energy as the surface tension coefficient times the surface area. This can be combined with an interface model to other approaches to model surface tension include both sharp and diffuse interface models. In sharp interface models the interface is calculated explicitly, while diffuse models infer the interface through the use of a phase field variable, such as concentration or density. Volume fractions can also be used to calculate curvatures of material interfaces and subsequent surface tension forces.

Diffuse interface surface tension models in expanding flows were studied using ALE–AMR [15]. An implicit surface tension model with interfacial flows is discussed in [16]. Variations of the volume-of-fluild (VOF) approach have been used to calculate surface tension effects by others [17,18]. An overview of diffuse interface methods and associated references can be found in reference [19]. A continuum method for surface tension is described by Brackbill, Kothe and Zemach [20]. This method identifies volume force that represents surface tension spread over a small but finite domain. This method, and its refinements provides the most useful and practical method for our code [21]. The height function approach has been used to calculate surface tension by many authors, e.g., [21,22] and various methods have been applied to reduce errors [23,24].

In this paper, we first describe the basic Lagrangian dynamics in ALE–AMR followed by a discussion of the surface tension models implemented in the code. We document our benchmarking studies including surface tension problems derived from the Young–Laplace equation, the Rayleigh instability and a variety of benchmarks using bubble. Analyses of the effects of mesh resolution and ALE are presented for the coalescing of a deformed bubble. Finally, we follow these benchmarks with some results from modeling EUV lithography experiments using the height-function surface tension approach.

2. Lagrangian dynamics

The equations of ALE–AMR use a staggered-grid, Lagrangian formulation with position and velocity being nodal variables and density, internal energy, temperature, pressure, strain, and stress being zonal (cell centered) variables. The thermal conduction and radiation transport equations are solved by implementing the diffusion approximation, which uses a nodal radiation energy and a zone-averaged nodal temperature. The plasma/fluid equations in a Lagrangian formulation (in vector and indicial notation $i, j, k = 1, 2, 3$) are:

$$\frac{\mathrm{D}\rho}{\mathrm{D}t} = -\rho\nabla\cdot\vec{U} = \rho U_{i,i} \tag{1}$$

$$\frac{\mathrm{D}\vec{U}}{\mathrm{D}t} = \frac{1}{\rho}\nabla\cdot\boldsymbol{\sigma} = \frac{1}{\rho}\sigma_{ij,j} \tag{2}$$

$$\frac{\mathrm{D}e}{\mathrm{D}t} = \frac{1}{\rho}V\boldsymbol{s}:\dot{\boldsymbol{\varepsilon}} - P\dot{V} = \frac{1}{\rho}V\left(s_{ij}\dot{\varepsilon}_{ij}\right) - P\dot{V} \tag{3}$$

where

$$\frac{\mathrm{D}}{\mathrm{D}t} = \frac{\partial}{\partial t} + \vec{U}\cdot\nabla$$

is the substantial derivative, ρ is the density, $\vec{U} = (u, v, w)$ is the material velocity, t is time, $\boldsymbol{\sigma}$ is the total stress tensor, P is the pressure, e is the internal energy, V is the relative volume ($\rho V = \rho_0$ where ρ_0 is the reference density), $\boldsymbol{s}$ is the deviatoric stress defined as,

$$s_{ij} = \sigma_{ij} + P\delta_{ij} \tag{4}$$

where δ is the Kronecker delta, and $\dot{\boldsymbol{\varepsilon}}$ is the strain rate tensor defined as

$$\dot{\varepsilon}_{ij} = \frac{1}{2}\left(\frac{\partial U_i}{\partial x_j} + \frac{\partial U_j}{\partial x_i}\right) \tag{5}$$

ALE–AMR uses a modified HEMP discretization [25–27] in evaluating the Lagrange update of the field variables. The interface reconstruction algorithm was originally developed to capture debris and shrapnel for high powered laser facilities and the details can be found in [28]. The VOF method and CALE93 (Tipton) algorithm [29] are used for the remapping of the Lagrangian grid. The remapping scheme is generally referred to as advection, due to its use of the advection equation, and is summarized well by Pember and Anderson [30]. During a simulation, the volume fraction of each material in a mixed zone is stored and the actual interface is only reconstructed as needed, such as during mesh refinement. Volume fractions in mixed zones are used for weighting the pressures, densities, stresses, etc., to obtain composite quantities. A void material with an associated volume fraction is introduced when a material failure occurs. Volume fractions are used during refinement of neighboring zones to determine the orientation of each interface and the actual location is determined by the volume fraction in the zone. Calculating the volume on either side of an interface in a 3D zone requires some effort, as the hexahedral zones are bounded on six sides by doubly-ruled surfaces [12]. Our approach is similar to that described by Kothe et al. [31]. A 2nd-order predictor-corrector model is utilized for time integration.

The strain rate tensor is evaluated using the numerical method proposed by Flanagan and Belytschko [32]. The scheme preferentially employs a monotonic artificial viscosity due to Christensen [33], and a kinematic hourglass filter [34].The pressure is determined by the equation of state (EOS), which returns pressure as a function of density and either energy or temperature. ALE–AMR provides access to a variety of analytic and tabular EOS, as well as user defined EOS implemented through Python functions. Stress deviators are determined by constitutive relations. For example, Hooke's Law for isotropic elastic materials is a linear relationship between deviatoric stress and deviatoric strain, given as

$$s_{ij} = 2\mu\varepsilon_{ij} \tag{6}$$

where μ is the shear modulus and ε is the strain tensor.

Addition of the full stress tensor terms for elastic-plastic flow to the basic Lagrangian equations in 1, 2, and 3D dimensions follows a straight-forward implementation of the equations given by Wilkins [25], using a finite difference formulation in the equations of motion. A correction is utilized to adjust the stress tensor for rotational effects and the stress tensor is remapped as six separate scalar values then reconstructed to ensure it remains deviatoric. The basic formulation of the stress tensor naturally provides a means of numerically including the effects of surface tension, particularly in the volume of fluid case.

For the regimes of interest where surface tension plays a role, it is not generally necessary to use separate electron and ion temperatures as is done in the more traditional ICF simulation codes [1–4]. ALE–AMR also does not include sliding interfaces, which are

unnecessary in the types of problems being targeted for simulation.

3. Surface tension models

The first surface tension model applied to ALE–AMR is a single-fluid, diffuse-interface, Korteweg-type model [35]. It is implemented by adding a third-order space derivative to the stress that is derived thermodynamically based on the Van der Waals–Cahn–Hilliard free energy. This approach is physically natural in that it does not make assumptions on the equation of state, but the surface width cannot be directly specified. The second approach is based on two-fluid VOF models, focusing on an implementation which calculates the curvature based on the height function approach [21]. Although this is a two fluid model, we implement a version that converts a single material density into the volume of fluid methodology and utilizes the same algorithm for a single-fluid implementation. The height function model is extended to three dimensions. The models are benchmarked using classical test cases, specifically the Laplacian equation, ellipsoid oscillation, and the Rayleigh–Plateau instability.

3.1. The single-fluid, diffuse-interface model

Here we describe the use of a Korteweg-type, single-fluid, diffuse interface model to simulate surface tension effects. The surface tension is modeled by adding an additional third-order stress term that can be thermodynamically derived from the Van der Waals–Cahn–Hilliard free energy. These surface tension models are complicated by the development of parasitic flow, a widely-faced, unwanted, numerically developed velocity field caused by an unbalance between numerically calculated stresses in interfacial regions [36].

The single-fluid diffuse interface model is applied by adding an additional tensor term to the governing equation. In Lagrangian form, the momentum equation is given by:

$$\rho \frac{D\vec{U}}{Dt} = -\nabla P + \nabla \cdot \boldsymbol{\tau_1} + \nabla \cdot \boldsymbol{\tau_2} \tag{7}$$

where $\boldsymbol{\sigma_1}$ is the viscous stress tensor:

$$\boldsymbol{\tau_1} = \mu\left(\nabla\vec{U} + (\nabla\vec{U})^T - \left(\frac{2}{3}\nabla\cdot\vec{U}\right)\boldsymbol{I}\right) \tag{8}$$

\boldmath τ_2 is the Korteweg-type surface tension stress tensor:

$$\boldsymbol{\tau_2} = K\left[\left(\frac{1}{2}(\nabla\rho)^2 + \rho\nabla\cdot(\nabla\rho)\right)\boldsymbol{I} - \nabla\rho\otimes\nabla\rho\right] \tag{9}$$

and K is a parameter related to the surface tension coefficient, γ, as given by:

$$\gamma = K\int_{-}^{+}\left(\frac{d\rho}{dz}\right)^2 dz, \tag{10}$$

where z is the normal direction of the interface and the integration is done across the interface. An EOS closes the system. In this model, the interfacial width cannot be explicitly defined, however if we define the interfacial width as ϵ, then $\epsilon \sim K\frac{\delta\rho^2}{\gamma}$.

However, standard discretizations lead to an imbalance in energy conservation that causes numerically-driven, parasitic flows. In this work, the standard, parasitic discretization of the surface tension stress tensor takes the form [35]:

$$\boldsymbol{\tau_2} = \begin{bmatrix} \rho\nabla^2\rho - \frac{1}{2}(\nabla\rho^x\otimes\nabla\rho^x - \nabla\rho^y\otimes\nabla\rho^y) & -\nabla\rho^x\otimes\nabla\rho^y & 0 \\ -\nabla\rho^x\otimes\nabla\rho^y & \rho\nabla^2\rho + \frac{1}{2}(\nabla\rho^x\otimes\nabla\rho^x - \nabla\rho^y\otimes\nabla\rho^y) & 0 \\ 0 & 0 & 2\rho\nabla^2\rho \end{bmatrix} \tag{11}$$

and the discretization that directly conserves energy takes the form [37]:

$$\boldsymbol{\tau_2} = \begin{bmatrix} \rho\nabla^2\rho + (\nabla\rho)^2 - \nabla\rho^x\otimes\nabla\rho^x & -\nabla\rho^x\otimes\nabla\rho^y & 0 \\ -\nabla\rho^x\otimes\nabla\rho^y & \rho\nabla^2\rho + (\nabla\rho)^2 - \nabla\rho^y\otimes\nabla\rho^y & 0 \\ 0 & 0 & \rho\nabla^2\rho + \nabla\left(\rho^2\right) \end{bmatrix} \tag{12}$$

where $(\nabla^2\rho)$ is calculated as the mean value of the square of the gradient, $\nabla\rho^y\otimes\nabla\rho^y$ is calculated as the square of the mean value of the gradient and $\nabla^2\rho$ is calculated using the gradient in both x and y directions.

This non-parasitic formulation can be derived directly from the Hamiltonian fluid mechanics and ensures that total energy

$$E = \int e(\rho, T) + \frac{1}{2}\rho|\vec{V}|^2 + \frac{K}{2}|\nabla\rho|^2 \tag{13}$$

is conserved. It will produce an incorrect equilibrium condition in cases without surface tension, but only because many fluid descriptions cannot handle evaporation and condensation well. A 4th-order, explicit Runge–Kutta method is applied for time integration.

Benchmarking of the Korteweg type model was made through the Young–Laplace equation, parasitic flow tests and droplet breakup simulations. The Young–Laplace equation is a nonlinear PDE that describes the capillary pressure difference across an interface due to surface tension [38]. To benchmark against the Young–Laplace equation we use a droplet surrounded by vapor of the same material, temperature, and similar pressure. Then we run the simulation until it reaches equilibrium, recording the difference of pressure between two sides of the interface. We measure the actual pressure difference and compare it against the Young–Laplace equation $\delta p = \frac{\gamma}{R}$ where γ is the surface tension coefficient measured as in Eq. (10). The simulation was performed using bubble radii of 0.15, 0.2, 025, 0.3, 0.35 and 0.4 cm with a K value of $1x10^{-6}$ (cm^7/g^*s^2). The simulation was ran for Aluminum at 6000 K using the Livermore tabular EOS, LEOS [39]. The results are plotted in Fig. 1. As seen, the surface tension behaves as expected and establishes the correct equilibrium pressure gradient across the surface.

The Young–Laplace benchmark can also be extended to study parasitic flow. The equilibrium droplet simulation is extended out to a longer time with the same initial conditions, comparing the formulations with and without parasitic flow removal. Kinetic energy is used as a measure of the remnant of the parasitic flow. The result is plotted in Fig. 2. Since parasitic flow is characterized by a non-zero velocity, the simulation with parasitic flow will not converge to a full equilibrium state, as shown by the red curve. However, the implementation of the non-parasitic method reduces the kinetic energy by 13 orders of magnitude over the course of the

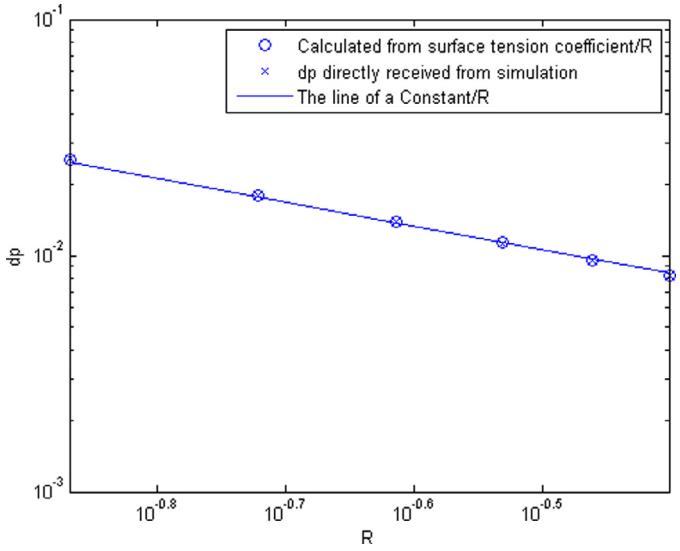

Fig. 1. Benchmark against the Young–Laplace equation. The x-axis is the radius of the droplet in cm and the y-axis is the pressure difference in erg/cc. Circle denotes the theoretical δp from Young–Laplace equation, and cross is the δp measured from simulation. The line is $\delta p = \gamma / R$ where γ is the surface tension coefficient.

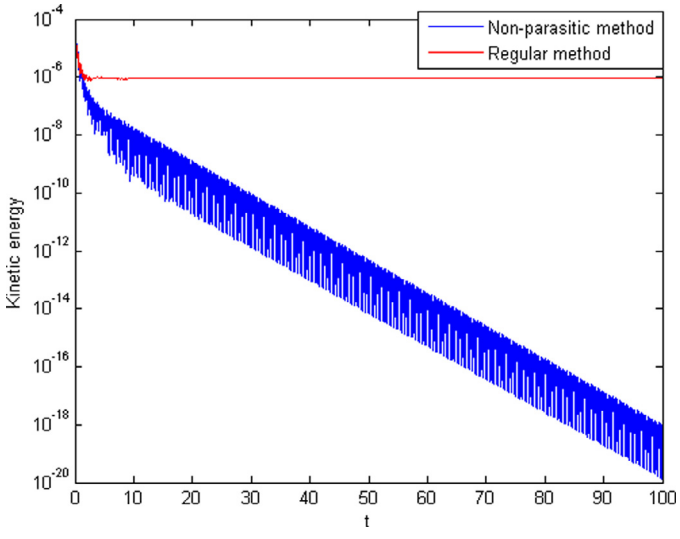

Fig. 2. Kinetic energy as a function of time, t. The x-axis is time in sec and y-axis is the kinetic energy in ergs. The red curve is a standard discretization while the blue curve is constructed to reduce parasitic flows. While the standard discretization still has substantial motion near equilibrium, the non-parasitic formulation has nearly eliminated any parasitic flow. (For interpretation of the references to color in this figure legend, the reader is referred to the web version of this article.)

simulation, yielding a flow field with negligible parasitic flows, as desired.

Droplet breakup is used as a simulation example for many numerical surface tension models but most of those simulations have an explicitly specified external force or shear flow that causes the breakup. In this study, we present a droplet breakup scenario caused only by heating. Depending on the temperature of the heated droplet: 1) if it is lower than the breakdown temperature, T_0, it will expand slightly before the decrease of internal pressure causes it to contract back to an equilibrium; or 2) if it is higher than T_0, the droplet will expand until it completely vaporizes. However, for our benchmark, we initialize the same droplet used in the Young–Laplace case to a temperature with a perturbation around T_0, causing part of the droplet to expand and part to retract. This instability causes the droplet to breakup as seen

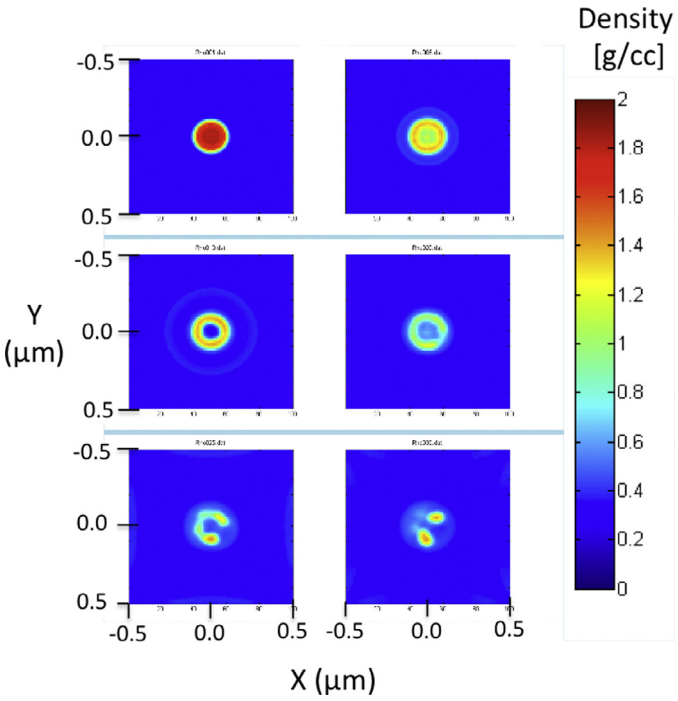

Fig. 3. Density plots of an aluminum droplet breakup simulation as result of heating. The axis are in units of cm^{-6} and the density scale is in units of g/cc.

in Fig. 3. This simulation uses a 10 nm radius aluminum droplet and was given an initial density of 2.5 g/cc with a background of aluminum vapor with a density of 0.1 g/cc and a surface tension parameter K of 0.001 (cm^7/g^*s^2). The perturbation was applied by randomly assigning each computational cell a temperature of around 6000 K. This cell-by-cell randomization was chosen because more structured perturbations can lead to a severe deformation of the bubble rather than a breakup for similar temperature variations.

Additionally, droplet formation can be tested by placing high pressure vapor inside an aluminum shell, as shown in Fig. 4. A 15 nm radius aluminum shell with a thickness of 2 nm was surrounded by aluminum vapor. This simulation was ran without surface tension and with $K = 1x10^{-6}$. While both results show material breakup due to physical instability of the spinodal region, the diffuse interface surface tension model forms the physically expected droplets and the case without surface tension does not.

While the diffuse-interface model has a number of beneficial features, the implied surface width can require a very small mesh size. This small mesh size can be appropriately modeled using AMR, but it forces the required time step to be too small to avoid significant computational cost in large-scale simulations. Therefore, this study was expanded to other potential surface tension models, as discussed in the next section.

3.2. Simulations with two-fluid volume-of-fluid models

We have also implemented three new volume-of-fluid surface tension models which calculate the surface tension by estimating the curvature from volume fraction. Calculating curvatures directly from volume fractions can result in surfaces that do not converge with mesh refinement and can have large errors. The three methods studied here that avoid this convergence problem are:

1) Convoluted VOF - stress form: A stress term calculated from the convoluted volume fraction is added to the stress term each time step.

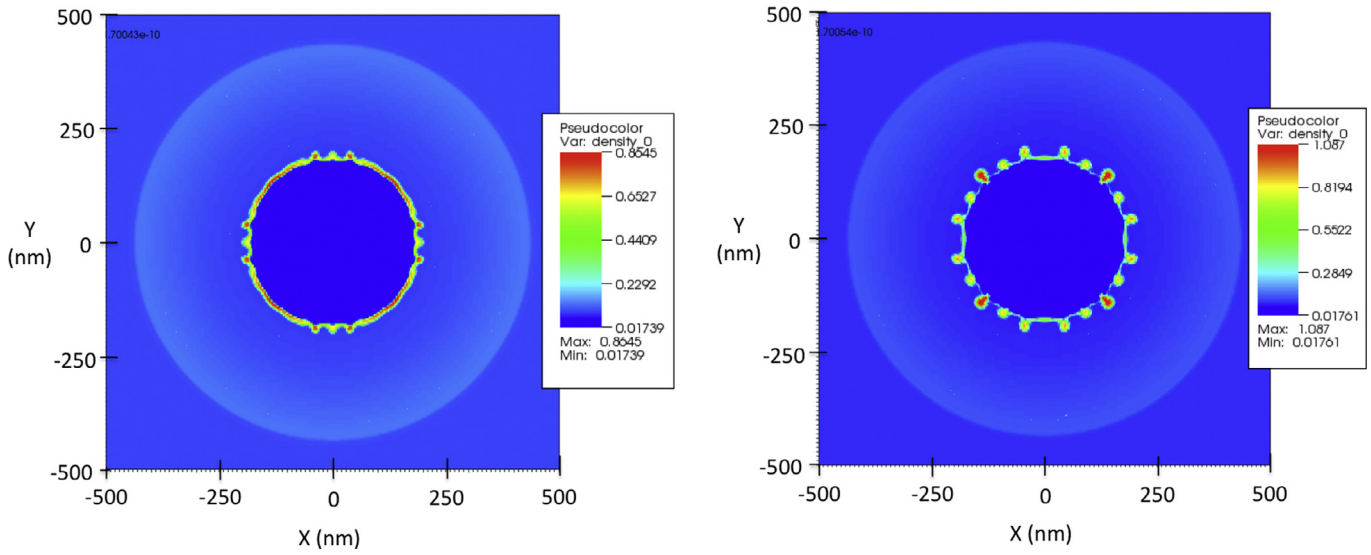

Fig. 4. Density plots of ALE–AMR simulations of an expanding 15 nm radius, 2 nm thick aluminum shell without a surface tension model (left) and with the diffuse interface surface tension model (right). The surface tension forms droplets as the shell expands.

2) Convoluted VOF - force form: A force term calculated from the convoluted volume fraction is implemented to update the velocity each time step.
3) Non-convoluted VOF - height function: A force term calculated from a non-convoluted volume fraction using a height function method which updates the velocity each time step.

Our tests revealed the convoluted methods to be ineffective for application to ALE–AMR. The convoluted approaches (1 & 2) use a smoothing kernel to convolute the Heaviside (VOF) function. The stress form can create large artificial acceleration in low-density cells as a result of the smoothing and the force form yields stability on kernel size but the problem is not stable when the mesh is small. Therefore, the height function method performs better for our application and is the focus for this study.

3.2.1. The height function approach

In the height function approach, a surface tension force is calculated as given by:

$$f = \gamma \kappa \vec{n}, \tag{14}$$

where γ is the constant surface tension coefficient, $\vec{n}$ is the outward normal from the interface and κ is the curvature, which is calculated by directly approximating the surface from volume fractions and applying vector calculus. The calculated force is then used to update nodal velocities. The height function approach is illustrated in Fig. 5:

In 2D, a quadratic fit with three points is used,

$$y(x) = h_1 x^2 + h_2 x + h_3 \tag{15}$$

and the curvature can then be calculated as:

$$\kappa = \nabla \cdot \left(\frac{\nabla y}{|\nabla y|} \right) = \frac{y''(x)}{\left(1 + [y'(x)]^2\right)^{3/2}} = \frac{2h_1}{(1 + h_2^2)^{1.5}}. \tag{16}$$

where y is the height of the surface, y' and y'' are the first and second derivative of the height function with respect to x, respectively, and h_1, h_2 and h_3 are constants found from the quadratic fit.

In 3D, we use a $3 \times 3 \times 7$ stencil and fit a 2D surface with a quadratic function using 6 points. In the example given in Fig. 5, the 2nd 3×7 stencil sits in the zy plane, yielding a height function of the form:

$$y(x, z) = h_1 x^2 + h_2 xz + h_3 z^2 + h_4 x + h_5 z + h_6 \tag{17}$$

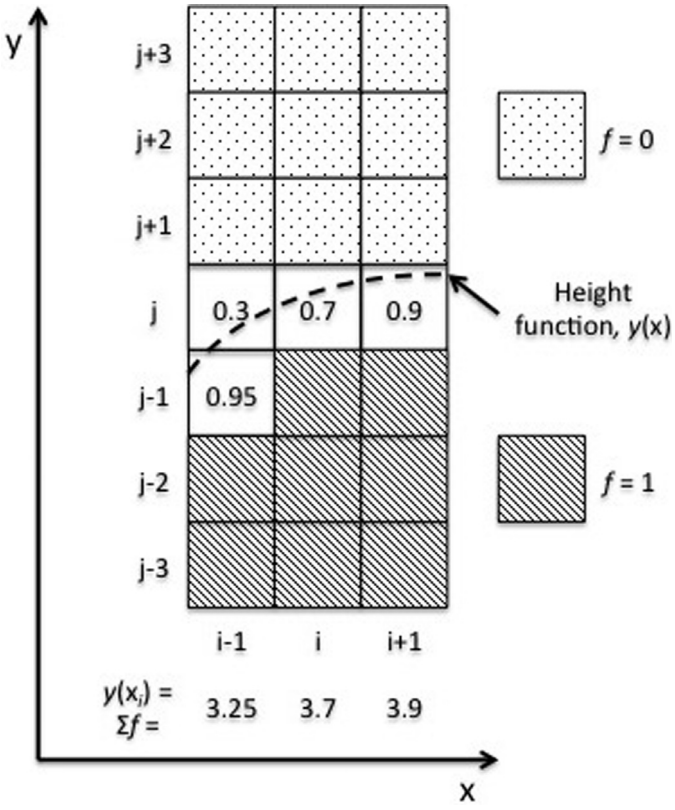

Fig. 5. The 2D, 3×7 stencil used to determine the height function. f, the volume fraction, is written in each cell where $0 < f < 1$. f is summed for each column and the values are used to calculate the height function, $y(x)$.

and a curvature given by:

$$\kappa = \nabla \cdot \left(\frac{\nabla y}{|\nabla y|} \right) = 2 \frac{h_1(1 + h_5^2) + h_2(1 + h_4)^2 - h_3 h_4 h_5}{(1 + h_4^2 + h_5^2)^{1.5}}. \tag{18}$$

The curvature is computed only in cells that possess an interface at the cell center and the calculation is made on the finest refined level of the mesh.

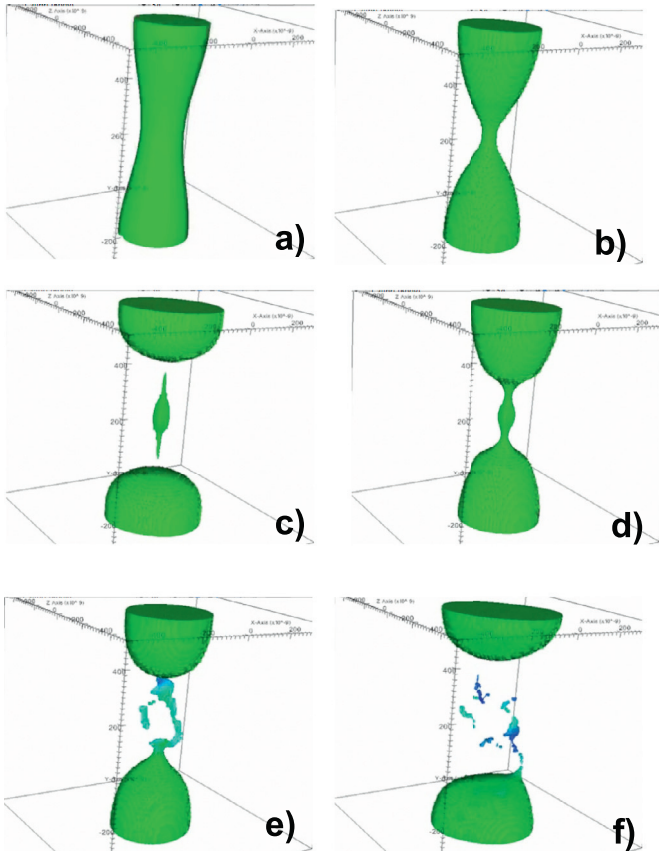

Fig. 6. Surface of liquid density shown over time for the Rayleigh instability benchmark. In a) we seen initial pinch, which narrows in b) and breakup is seen in c) followed by oscillation in d–f.

Height functions are one way to deal with the fact that volume fractions abruptly vary through the interface, transitioning from one material and/or value to another over a cell width. While the height function and curvature are calculated on the finest grid at cell centers, the force is calculated in nodes using curvature values from the adjacent cells. We found the height function approach to be relatively easy to implement, with second-order accuracy in Eulerian mode and good computational efficiency. When applying non-structured meshes, the order of accuracy of the current implementation is uncertain, but it has been shown that volume of fluid non-uniform meshes can be guaranteed second-order by using three height columns for each calculation [40]. While our current implementation of the height function approach works well for Eulerian and modestly distorted ALE meshes, extension such as suggested in [40] would be beneficial for more distorted meshes.

One benchmark chosen for the height function methodology is the Rayleigh instability [41]. This benchmark is illustrated in Fig. 6. In a 3D geometry, we start with a liquid tube with an initial pinch, which is unstable. The aluminum tube has a diameter of 35 nm and the initial pinch reduces the diameter of the tube by half at the center. The aluminum has a temperature of 6000 K and the initial liquid tube and surrounding vapor densities are 1.6 and 0.2 g/cc, respectively. The surface tension coefficient is set at a higher than typical value, 1000 mN/n, to enhance the surface tension effects for illustrative purposes. The pinch causes the nearby liquid to oscillate and thin until the surface breaks, leaving two large droplets on either side of the pinch and a dissipation of any material left in-between, as expected.

Mesh convergence was tested by modeling the convergence of a misshaped bubble into its stable circular shape. The bubble is constructed by overlaying the bubble with an identical bubble of background vapor that overlaps 30% of the bubble's diameter. The aluminum bubble has a diameter of 60×10^{-6} cm, a density of 1.5 g/cc and surface tension coefficient of 1000 mN/m. It is surrounded by an aluminum vapor with a density of 0.1 g/cc and the temperature field of the domain is 6000 K. The time progression of the coalescence is given in Fig. 7 for a bubble with 108 cells across its diameter. Without surface tension, the crescent shaped liquid region develops a gradient at its boundary to reach an equilibrium with the background but otherwise shows no change in shape, regardless of the mesh. However, with surface tension turned on the bubble reacts to fill the missing piece of the circular pattern, overshoots and oscillates into a final circular shape.

A mesh convergence analysis for this case is given in Fig. 8 through the comparison of the bubble contour of density 0.9 g/cc for bubbles with 108, 54, 40 and 27 cells across their diameters. The bubble remains quite consistent during the initial filling of the crescent hole through 4×10^{-9} s. Then, the smaller meshes begin to show significant deviations due to variations in the numerical diffusion as the bubble oscillates into its final circular shape. However, proper refinement minimizes the contour differences in the finest meshes, yielding a consistent result. The effects of ALE can also be explored with the coalescing bubble. Due to the inward surface tension forces, the primary mesh motion is the compression and expansion of cells rather than shearing. This makes the coalescing bubble a particularly stable ALE case, as the mesh skewness remains under 10% throughout the simulation. A comparison of the Eulerian and ALE contours of density 0.9 g/cc for the 108 cell case is given in Fig. 9. The ALE solution is almost identical to the Eulerian result and completed approximately 30% faster. This shows that with a strict remapping scheme, the volume of fluid model is capable of accurate modeling with ALE.

4. Application to EUV lithography

The height function approach to modeling surface tension has been successfully applied to an ALE–AMR simulation of EUV lithography. Laser-produced-plasma sources are being developed for semiconductor manufacturing. One approach uses pulses of high power CO_2 laser light focused onto small, molten tin droplets, which heat the tin to a very high temperature. The highly ionized tin plasma radiates over a broad range of wavelengths and the 13.5 nm light, which is of interest for microchip manufacturing, is collected by a large ellipsoidal, multilayer mirror. In order to improve efficiency, researchers at ASML have developed a pre-pulse technique where an initial low energy pulse is used to expanded the droplet before the main pulse [42]. This process is illustrated in the left image of Fig. 10 and the initial deformation of a tin droplet via pre-pulse laser heating is shown in the right images. This pre-pulse simulation was completed using HYDRA, a radiation plasma physics code developed at Lawrence Livermore National Laboratory. The log scale on density allows one to see the low density plasma surrounding the droplet, which is initially only on the side facing the laser, as seen in the top figure.

The result from the pre-pulse simulation is transferred to ALE–AMR to complete the hydrodynamic drift-phase simulation. This case was simulated using 3 levels of refinement with a finest mesh size of 1×10^{-5} cm in Eulerian mode to ensure there is no mesh entangling as the liquid bubble thins into a film and twists throughout the domain. The tin EOS table using in this work was constructed using the approaches outlined in references [43,44] using the data from reference [45]. The two-phase equilibrium model, in which the Maxwell loops were removed, was used in this work. The drift-phase results are illustrated in Fig. 11, where the density variation is shown after 0.3 μs on the left and 1.5 μs on the right. The mesh is shown in the lower left image, where

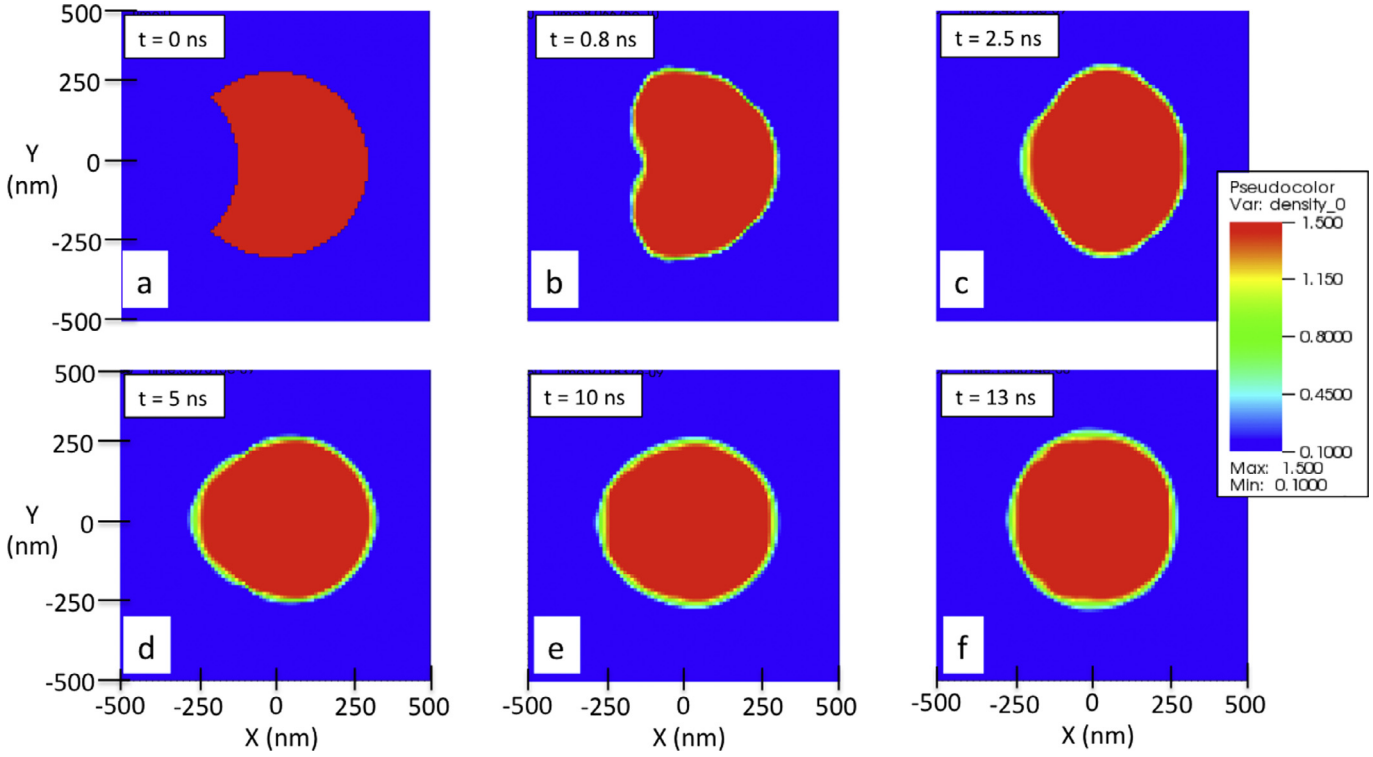

Fig. 7. Coalescing bubble density shown over time. The initial bubble is given by (a), fills the crescent void and overshoots (b)–(d) and rebounds to a nearly circular shape (e) and (f).

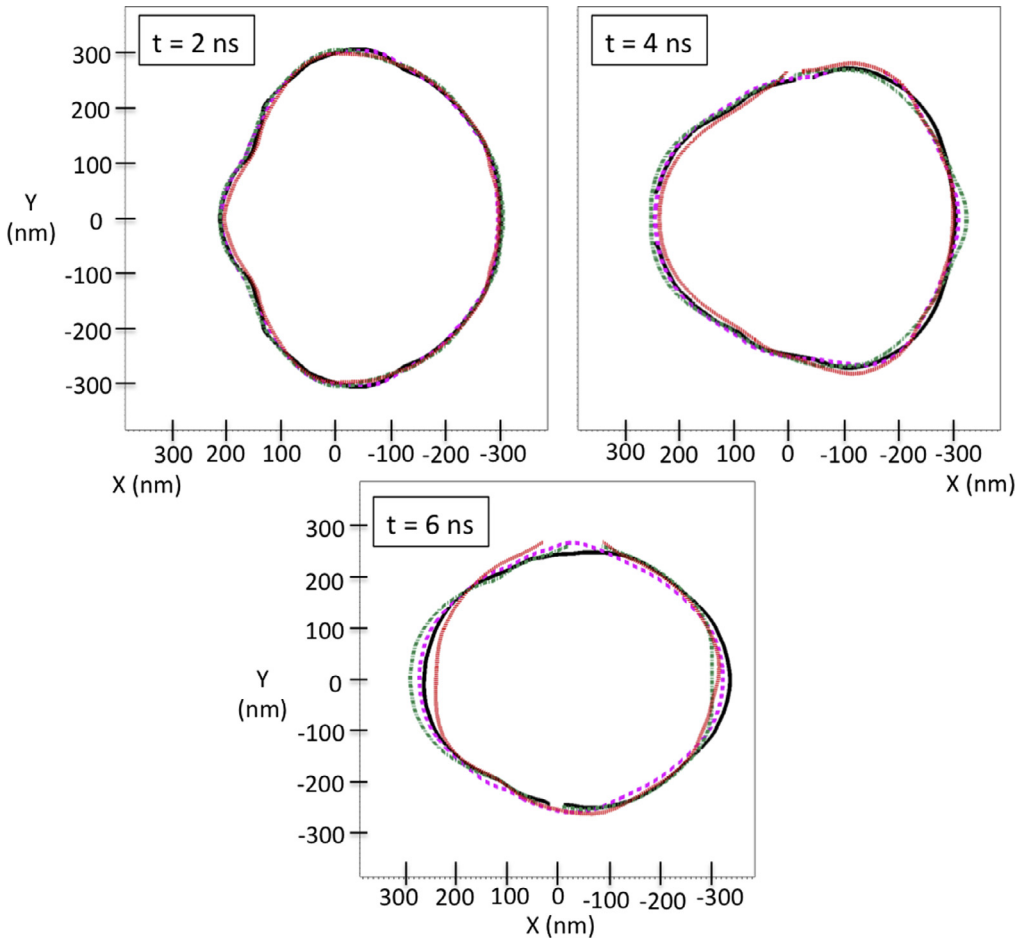

Fig. 8. Comparison of density 0.9 g/cc contours over time. The solid black line is a bubble starting with 108 cells, the dark red dashed line is 54 cells, the green dot-dash line is 40 cells, and the red line is 27 cells. (For interpretation of the references to color in this figure legend, the reader is referred to the web version of this article.)

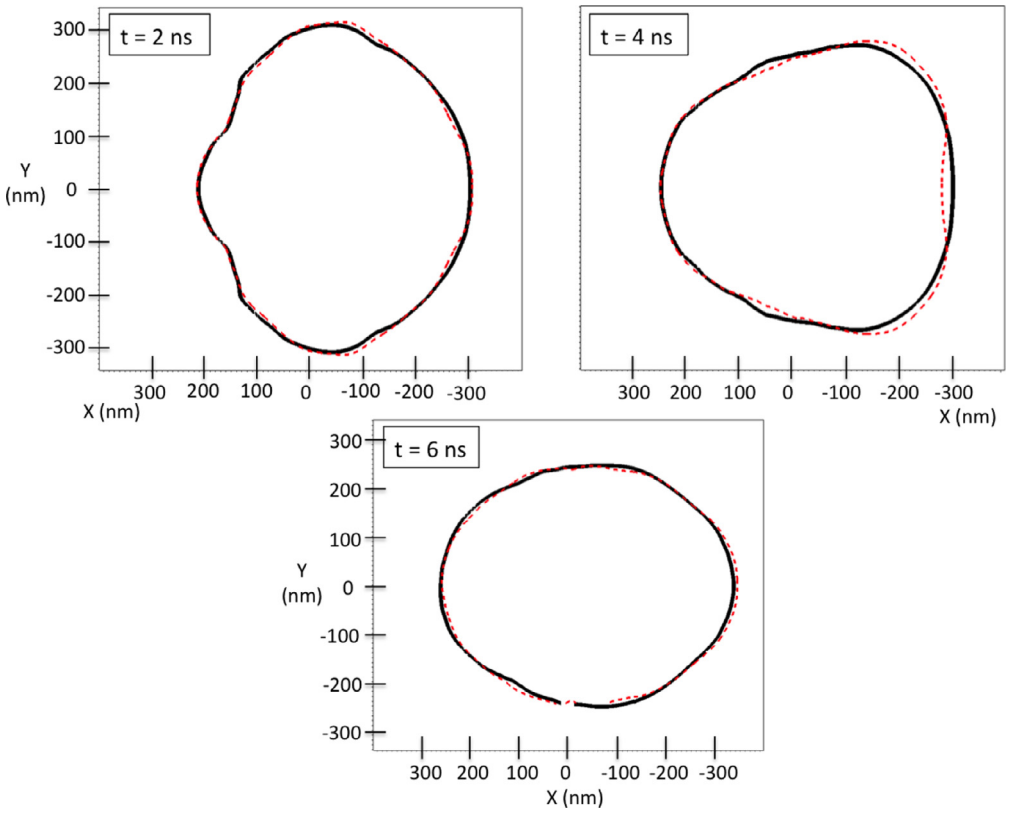

Fig. 9. Comparison of density 0.9 g/cc contours over time for a diameter of 108 cells. The black line is the Eulerian solution and the red line is a solution with ALE. (For interpretation of the references to color in this figure legend, the reader is referred to the web version of this article.)

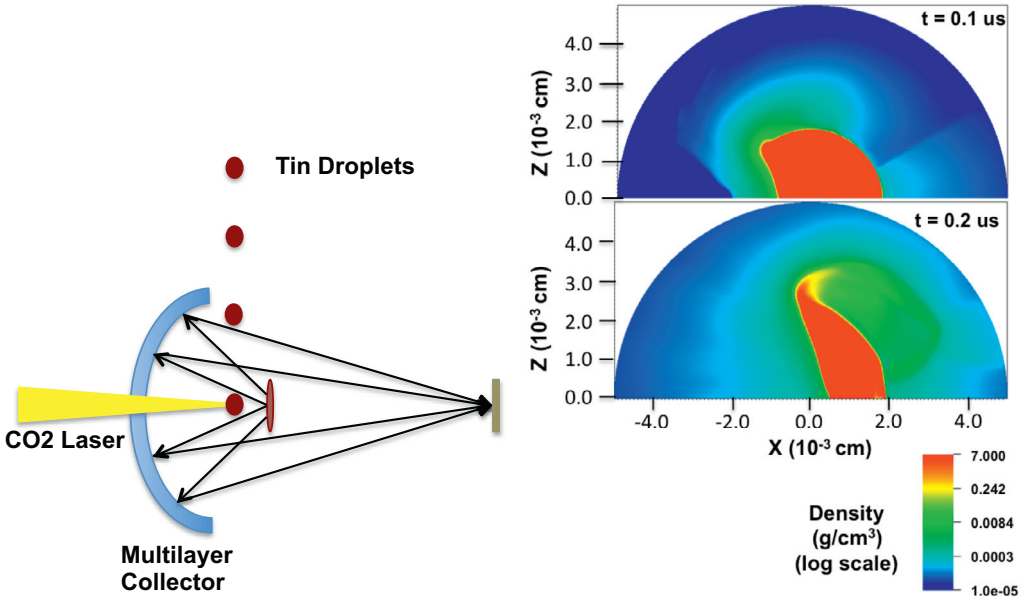

Fig. 10. Left: EUV lithography source using tin droplets heated by CO2 laser with a pre pulse to flatten droplet and EUV radiation collected by multi-layer mirror. Right: simulation of initial flattening of tin droplet by pre-pulse. The pre-pulse simulation was performed at LLNL and then transferred to ALE–AMR for hydrodynamic analysis of the drift phase.

the finest detail is concentrated on the liquid/vapor interface. After the drift period the "droplet" continues to expand and becomes very thin. The comparison of the drift simulations with and without surface tension are shown in the right-hand images. While the effects of surface tension are not dramatic, it is clear that surface tension predicts a smoother, more realistic liquid surface. The use of the volume-of-fluid surface tension model in ALE–AMR for this simulation only added a modest ($\approx$ 20%) increase in the computational cost of the simulation.

Further studies of EUV are being conducted that utilize a more powerful pre-pulse beam. The more powerful prepulse flattens the Tin bubble considerably faster, which requires simulations to in-

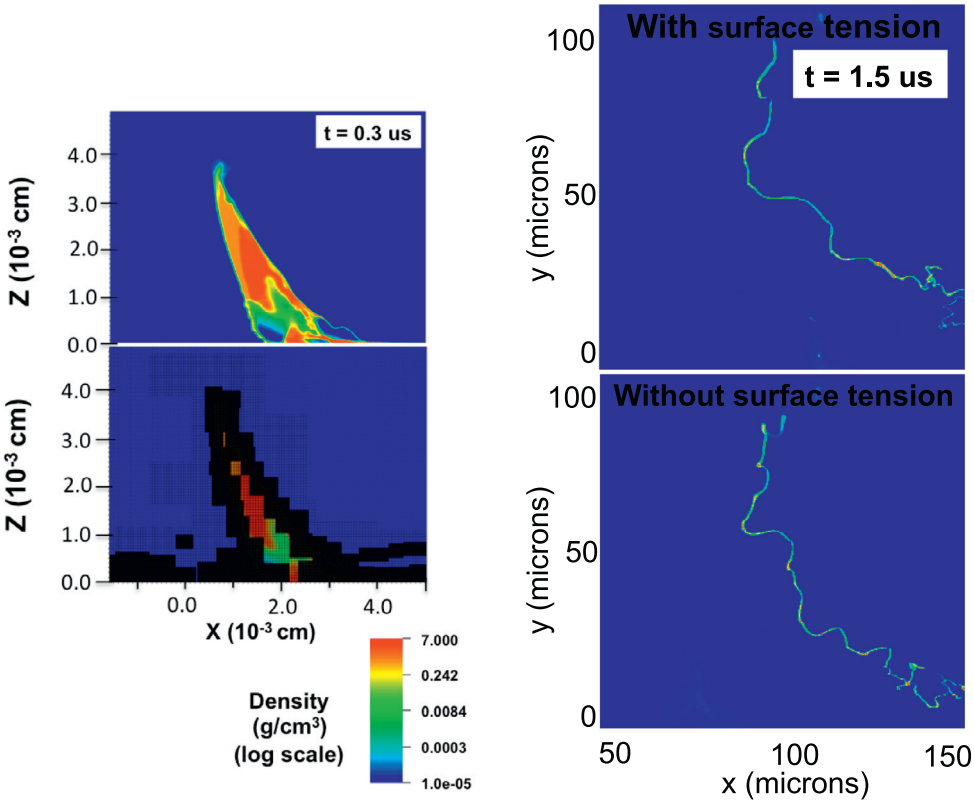

Fig. 11. Left: ALE–AMR simulation showing density variation within droplet in upper image and AMR mesh in lower image. Right: late time simulation of tin droplet with and without surface tension. The laser hits the droplet from the left.

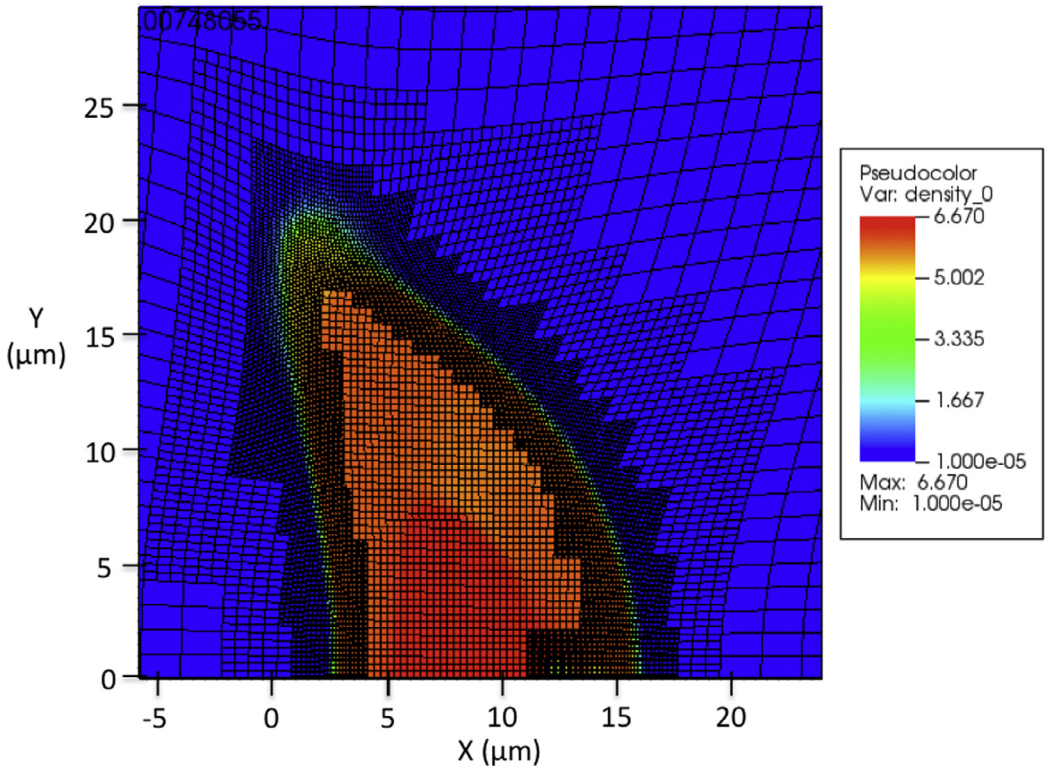

Fig. 12. Close-up of the skewed mesh near the tin droplet in an ALE-based EUV simulation. The color denotes the tin density. (For interpretation of the references to color in this figure legend, the reader is referred to the web version of this article.)

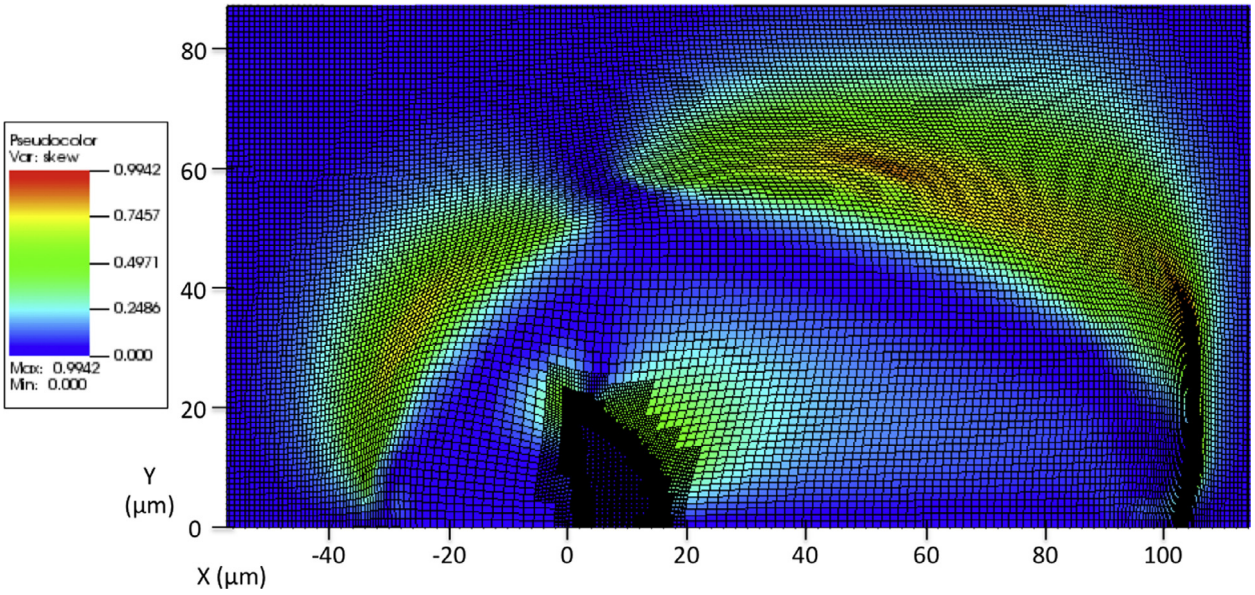

Fig. 13. Right: an overview of the mesh in an ALE-based EUV simulation. The color denotes the mesh skewness. Similar profiles develop in the tin vapor throughout the simulation. (For interpretation of the references to color in this figure legend, the reader is referred to the web version of this article.)

clude finer meshing earlier and increased refinement over larger regions of the domain. For these more complex simulations, ALE is being explored to determine if it can substantially improve wall-time. A characteristic ALE mesh for an EUV simulation can be found in Fig. 12. Initial investigations show that ALE can work effectively near the liquid surface and yield results comparable with a pure Eulerian case. However, the Tin vapor dominates the mesh skewness due to the surrounding low pressure environment, as shown in Fig. 13. This currently prevents ALE from substantially improving runtime by drastically increasing the frequency of remapping. Overall, a pure Eulerian methodology is currently preferred because it reduces the possibility of mesh tangling or substantial time step reductions in the vapor field with guaranteed second-order accuracy in exchange for a modest increase in computational costs. More in-depth investigations are currently ongoing to determine whether a carefully selected ALE remapping criteria can improve simulation performance for these complex hydrodynamic simulations or if an improved curvature calculation methodology can be utilized to guarantee accuracy on more severely skewed meshes.

5. Conclusions

Several surface tension models where applied to the 3D multi-physics, multi-material code ALE–AMR. Benchmarking studies show expected, accurate results for all models, but also demonstrate limitations that prevent their application to current simulations of interest. A single-fluid, diffuse-interface, Van der Waals–Cahn–Hilliard free energy model creates stable droplets that match the solution of the Young–Laplace equation. Numerically removing parasitic flows using the methods of Jamet et al. [37] is effective for this model. However, this diffuse-interface model can require a very small mesh size to resolve the surface width, which results in significant computational cost when implemented the full-scale simulations that are of primary interest to the ALE–AMR code.

These limitations motivated consideration of additional surface tension models that estimating the curvature from volume fractions. This study found that a height function approach in conjunction with a volume-fraction interface reconstruction package is optimal for the current droplet dynamics studies of EUV lithography. The addition of surface tension in the simulation is possible with only a modest increase in computational cost. Future work in the area of EUV lithography will include droplet dynamics associated with radiation and modeling debris remaining from a previous droplet that can deform future droplets, a study which is dominated by surface tension forces.

Acknowledgments

We acknowledge the National Energy Research Scientific Computing Center, supported by the Office of Science, U.S. Department of Energy under Contract No. DE-AC02-05CH11231. Work by LBNL under DE-AC02-05CH11231 was supported by the Director, Office of Science of the U.S. Department of Energy and the Petascale Initiative in Computational Science and Engineering. Work by LLNL was performed under the auspices of the U.S. Department of Energy by Lawrence Livermore National Security, LLC, Lawrence Livermore National Laboratory under Contract DE-AC52-07NA27344.

References

[1] Breil J, Galera S, Maire P-H. Multi-material ale computation in inertial confinement fusion code chic. Comput Fluids 2011;46:161–7.
[2] Zimmerman GB, Kruer WL. Lasnex paper. Comments Plasma Phys Control Fusion 1975;2:51.
[3] Marinak MM, Haan SW, Dittrich TR, Tipton RE, Zimmerman GB. A comparison of three-dimensional multimode hydrodynamic instability growth on various national ignition facility capsule designs with hydra simulations. Phys Plasmas 1998;5:1125.
[4] Holstein PA, et al. Target physics for the megajoule laser (LMJ). Nucl Fusion 2004;44:S177–84.
[5] Koniges A, Masters N, Fisher A, Eder D, Liu W, Anderson R, et al. Multi-material ALE with AMR for modeling hot plasmas and cold fragmenting materials. Plasma Sci Technol 2015;17:117.
[6] Colella P. Multidimensional upwind methods for hyperbolic conservation laws. J Comput Phys 1990;87.
[7] Anderson RW, Elliott NS, Pember RB. An arbitrary Lagrangian–Eulerian method with adaptive mesh refinement for the solution of the Euler equations. J Comput Phys 2004;199:598–617.
[8] Hornung R, Kohn S. Managing application complexity in the Samrai object-oriented framework. Concurrency 2002;14:347–68.
[9] Fisher A, Masters N, Dixit P, Benson D, Koniges A, Anderson R, et al. Hierarchical material models for fragmentation modeling in NIF-ALE-AMR. J Phys 2008;112:022027.
[10] Eder DC, Fisher AC, Koniges AE, Masters ND. Modelling debris and shrapnel generation in inertial confinement fusion experiments. Nucl Fusion 2013;53:113037.

[11] Koniges AE, et al. Modeling warm dense matter experiments using the 3d ALE-AMR code and the move toward exascale computing. EPJ Web Conf 2013;59:09006.
[12] Koniges A, Debonnel C, Andrew J, Eder D, Kalantar D, Masters N, et al. Experiments for the validation of debris and shrapnel calculations. J Phys 2008;112:032072.
[13] Eder D, Bailey D, Bertozzi A, Fisher A, Koniges A, Liu W, et al. Late-time numerical simulations of high-energy-density (hed) targets Twenty second international conference on numerical simulations of plasmas; 2011. (Presentation).
[14] Schafgans AA, Brown DJ, Fomenkov IV, Sandstrom R, Ershov A, Vaschenko G, et al. Advancements in predictive plasma formation modeling. In: Proc. SPIE 9776. Extreme Ultraviolet (EUV) Lithography VII; 2016. 97760K–97760K.
[15] Liu W, Bertozzi AL, Kolokolnikov T. Diffuse interface surface tension models in an expanding flow. Comm Math Sci 2012;10(1):387–418.
[16] Hysing S. A new implicit surface tension implementation for interfacial flows. Int J Numer Methods Fluids 2006;51(6):659–72.
[17] Gauer M, Hannemann V, Hannemann K. Implementation of the VOF method in the DLRTAU code. In: 45th AIAA/ASME/SAE/ASEE joint propulsion conference & exhibit; 2009. p. 4863.
[18] Denner F, van Wachem BG. Fully-coupled balanced-force VOF framework for arbitrary meshes with least-squares curvature evaluation from volume fractions. Numer Heat Transfer Part B 2014;65(3):218–55.
[19] Anderson D, McFadden GB, Wheeler A. Diffuse-interface methods in fluid mechanics. Annu Rev Fluid Mech 1998;30(1):139–65.
[20] Brackbill JU, Kothe DB, Zemach C. A continuum method for modeling surface tension. J Comput Phys 1992;100:335–54.
[21] Cummins SJ, Francois MM, Kothe DB. Estimating curvature from volume fractions. Comput Struct 2005;83:425–34.
[22] Afkhami S, Bussmann M. Height functions for applying contact angles to 3d VOF simulations. Int J Numer Methods Fluids 2009;61(8):827–47.
[23] López J, Hernández J. On reducing interface curvature computation errors in the height function technique. J Comput Phys 2010;229(13):4855–68.
[24] Malik M, Fan ES-C, Bussmann M. Adaptive VOF with curvature-based refinement. Int J Numer Methods Fluids 2007;55(7):693–712.
[25] Wilkins ML. Computer simulation of dynamic phenomena. Springer Verlag; 1999.
[26] Wilkins ML. Use of artificial viscosity in multidimensional fluid dynamic calculations. J Comput Phys 1980;36:281–303.
[27] Pember RB, Anderson RW. A comparison of staggered-mesh lagrange plus remap and cell- centered direct Eulerian Godunov schemes for Eulerian shock hydrodynamics. Nuclear Explosives Code Developers Collaborations (NECDC) 2000 UCRL-JC-139820. Lawrence Livermore National Laboratory; 2000.
[28] Masters ND, ND, Anderson R, Elliot N, Fisher A, Gunney B, et al. Interface reconstruction in two-and three-dimensional arbitrary Lagrangian–Eulerian adaptive mesh refinement simulations. J Phys 2008;112:022017.
[29] Jun B. A simple advection scheme for material interface. Tech. Rep.. UCRL-JC-139912, Lawrence Livermore National Laboratory; 2011.
[30] Pember R, Anderson R. Comparison of direct Eulerian Godunov and Lagrange plus remap, artificial viscosity schemes. Proc 15th American institute of aeronautics and astronautics computational fluid dynamics conference, Anaheim, CA; 2001.
[31] Kothe D, Williams M, Lam K, Korzekwa D, Tubesing P, Puckett E. A second-order accurate, linearity-preserving volume tracking algorithm for free surface flows on 3d unstructured meshes. In: Proceedings of the 3rd ASME/JSME joint fluids engineering conference, San Francisco, CA. Citeseer; 1999. p. 18–22.
[32] Flanagan D, Belytschko T. A uniform strain hexahedron and quadrilateral with orthogonal hourglass control. Int J Numer Methods Eng 1981;17:679–706.
[33] Christensen R. Godunov methods on a staggered mesh an improved artificial viscosity. Technical Report UCRL-JC-105269. Lawrence Livermore National Laboratory; 1990.
[34] Margolin L, Pyun J. A method for treating hourglass patterns. Technical Report LA-UR-87-439. Los Alamos National Laboratory; 1987.
[35] Nadiga BT, Zaleski S. Investigations of a two-phase fluid model. Eur J Mech B 1996;15:885–96.
[36] Lafaurie B, Nardone C, Scardovelli R, Zaleski S, Zanetti G. Modelling merging and fragmentation in multiphase flows with surfer. J Comput Phys 1994;113:134–47.
[37] Jamet D, Torres D, Brackbill J. On the theory and computation of surface tension: the elimination of parasitic currents through energy conservation in the second-gradient method. J Comput Physics 2002;182:262–76.
[38] Padula M. On the exponential decay to the rest state for a viscous isothermal fluid. J Fluid Mech Anal 1998;1(1):62–73.
[39] Young D, Corey E. Release of new leos equation of state library. Lawerence Livermore National Laboratory unpublished memo; 1998.
[40] Francois M, Swartz B. Interface curvature via volume fractions, heights and mean values on nonuniform rectangular grids. J Comput Physics 2010;229(2):527–40.
[41] Mason G. An experimental determination of the stable length of cylindrical liquid bubbles. J Colloid Interface Sci 1970;32:172.
[42] Schafgans AA, Brown DJ, Fomenkov IV, Sandstrom R, Ershov A, Vaschenko G, et al. Performance optimization of MOPA pre-pulse LPP light source SPIE advanced lithography. International Society for Optics and Photonics; 2015. 94220B–94220B.
[43] More RM, Warren KH, Young DA, Zimmerman GB. A new quotidian equation of state (QEOS) for hot dense matter. The Physics of Fluids 1988;31(10):3059–78.
[44] Young DA, Corey EM. A new global equation of state model for hot, dense matter. Journal of Applied Physics 1995;78(6):3748–55.
[45] Young DA. Phase diagrams of the elements. Univ of California Press; 1991.